Journal of Materials Chemistry A

PAPER

View Article Online
View Journal | View Issue

Cite this: J. Mater. Chem. A, 2015, 3, 2794

Synthesis of TiO_2 decorated Co_3O_4 acicular nanowire arrays and their application as an ethanol sensor†

Liqiang Zhang,[ab] Zhenfei Gao,[ab] Chao Liu,[a] Yunhan Zhang,[a] Zhiqiang Tu,[a] Xiaopeng Yang,[c] Fan Yang,[a] Zhen Wen,[d] Liping Zhu,[d] Rui Liu,[e] Yongfeng Li*[a] and Lishan Cui*[ab]

Received 25th November 2014
Accepted 10th December 2014

DOI: 10.1039/c4ta06440b

www.rsc.org/MaterialsA

A novel heterostructure of TiO_2 modified Co_3O_4 (TiO_2/Co_3O_4) acicular nanowire (NW) arrays has been fabricated in this study, which demonstrates a good performance for ethanol detection at working temperatures as low as 160 °C. Co_3O_4 NW arrays were first grown on an Al_2O_3 substrate patterned with an Ag/Pd electrode by a hydrothermal method, and then TiO_2 nanoparticles were decorated on the surface of Co_3O_4 NW arrays by using pulsed laser deposition (PLD). It is found that after decoration of TiO_2, the TiO_2/Co_3O_4 NW array sensor exhibits a much higher response to ethanol ($R_g/R_a = 65$, R_g is the sensor resistance measured in a mixture of target gases and R_a is the resistance measured in air) compared with the pristine Co_3O_4 NW sensor ($R_g/R_a = 25$). Importantly, the TiO_2/Co_3O_4 sensor has shown a detection limit as low as 10 ppm, and a good reproducibility. The reason for the enhanced sensing properties of TiO_2/Co_3O_4 is considered to be due to the formation of a p–n junction between the p-type Co_3O_4 and n-type TiO_2.

1. Introduction

Co_3O_4 is an important semiconductor with a normal spinel structure, which has been widely studied as a promising material applied in lithium-ion batteries, supercapacitors, catalysis, *etc.*[1–6] Among its numerous applications, Co_3O_4 based gas sensors have attracted much attention recently, which exhibit good gas-sensing characteristics.[7–14] To optimize the gas performance of Co_3O_4, a large amount of effort has been made to control the morphology and size of Co_3O_4 in the previous studies.[8,13,15,16] The synthesis of various nanostructures of Co_3O_4 such as nanoparticles,[17] nanorods,[6,7] nanofibers,[10,18,19] nanosheets[20] and hollow nanospheres[9] has been carried out by using varieties of techniques including electrospinning,[18] hydrothermal methods,[12] solid state thermal decomposition, *etc.*[17,20] Among these Co_3O_4 based nanomaterials, a one-dimensional nanowire array is considered to be a promising architecture with a high chemical response.[21] Yoon *et al.* have prepared Co_3O_4 nanofibers with one-dimensional morphologies by electrospinning, which exhibited a high response to 100 ppm C_2H_5OH at 300 °C.[10] Wen *et al.* have synthesized one-dimensional rhombus-shaped Co_3O_4 nanorod arrays *via* a hydrothermal route, which showed a high sensitivity to ethanol up to ~70.[12] As we know, designing a heterojunction structure between different band gap and energy level semiconducting materials is an effective way to enhance the photocatalytic and catalytic activity, and gas sensing performance of the nanocomposite material.[2,22–24] Recently, it has been found that designing a p–n junction by combining Co_3O_4 with other n-type semiconductors would be a significant route to enhance its gas response.[12,25–28] In the heterogeneous region, the p-type semiconductor Co_3O_4 and the n-type semiconductor TiO_2 can form a self-built electric field, and establish a depletion layer. When exposed to air, the hole density on the surface of the Co_3O_4 increase while the electrons on the surface of the TiO_2 decrease due to the ionization of absorbed oxygen species, which leads to a lower resistance of the Co_3O_4. When ethanol was introduced into the chamber, the electrochemical reaction between oxygen and gas molecules will be quickly neutralized with more holes.

[a]State Key Laboratory of Heavy Oil Processing, China University of Petroleum, Beijing 102249, China. E-mail: yjfli@cup.edu.cn; lishancui63@126.com; Fax: +86-010-89739028; Tel: +86-010-89739028

[b]Department of Materials Science and Engineering, China University of Petroleum, Beijing 102249, China

[c]School of Materials Science and Engineering, University of Jinan, Jinan 250022, China

[d]State Key Laboratory of Silicon Materials, Department of Materials Science and Engineering, Zhejiang University, Hangzhou 310027, China

[e]State Key Laboratory of Environmental Chemistry and Ecotoxicology, Research Center for Eco-Environmental Sciences, Chinese Academy of Sciences, Beijing 100085, China

† Electronic supplementary information (ESI) available: The optical micrographs of the Al_2O_3 substrates, the as-synthesized precursor, pristine Co_3O_4 and TiO_2/Co_3O_4 NW arrays; the image of the gas sensing analysis system; the response curve of the TiO_2/Co_3O_4 sensor to several other gases; the SEM image of the cobalt-precursor nanostructure growing on the Al_2O_3 substrate at different hydrothermal temperatures; the *I–V* characteristics of the TiO_2/Co_3O_4 sample between the two neighboring electrodes; the gas responses of the TiO_2/Co_3O_4 sensor to a series of TiO_2 contents. See DOI: 10.1039/c4ta06440b

But at this moment, the electron transfer from n-type TiO_2 to p-type Co_3O_4 is impeded because of energy band bending, which makes the resistance of the TiO_2/Co_3O_4 demonstrate a more obvious change than the pristine Co_3O_4. As a consequence, it demonstrates a higher gas sensitivity than the pristine Co_3O_4. Based on the above discussion, controlling the morphology and building a p–n junction at the same time is expected to be an effective way to enhance its gas response. However, such a kind of important and interesting topic has not yet been fully investigated.

In this study, we report the synthesis of Co_3O_4 acicular NW arrays with acicular morphology *via* a facile hydrothermal route. TiO_2 nanoparticles were subsequently decorated on the Co_3O_4 NW by using pulsed laser deposition (PLD) and formed a p–n junction with it. The gas sensing performance was systematically investigated and compared with the pristine Co_3O_4 acicular NW arrays. It is found that the TiO_2 decorated Co_3O_4 nanocomposite shows a much better sensing performance than the pristine Co_3O_4 NW arrays.

2. Experimental details

The synthesis of TiO_2/Co_3O_4 NW arrays includes two steps, one is preparing Co_3O_4 acicular NW arrays on an Al_2O_3 substrate by using the hydrothermal route, and the other is decorating TiO_2 nanoparticles on the surface of Co_3O_4 by using PLD. In a typical procedure for fabricating the Co_3O_4 acicular NW arrays, 4 mmol (1.16 g) of cobalt nitrate ($Co(NO_3)_2 \cdot 6H_2O$), 8 mmol (0.29 g) ammonium fluoride (NH_4F) and 8 mmol (1.12 g) of urea ($CO(NH_2)_2$) as sources were dissolved in 40 ml deionized (DI) water under stirring at room temperature. In the synthesis of acicular Co_3O_4 NWs, the roles of NH_4F and $(CO(NH_2)_2)$ have already been discussed in detail in a previous study.[29] After stirring for 20 min, the homogeneous solution was transferred into a 100 ml Teflon lined stainless steel autoclave. A piece of polycrystalline Al_2O_3 ceramic plate substrate (13.4 mm × 7 mm, 0.5 mm in thick) that had been plated with a Ag/Pd finger region (five pairs, both the width and distance are 200 μm) as electrode was immersed in the reaction solution against the bottom of the autoclave. The polycrystalline alumina ceramic substrates were bought from Beijing Elite Tech Co., Ltd, China. As the amount of Co_3O_4 NW arrays deposited on the Pd–Ag electrode substrates is not enough for the BET detection, we also took another piece of cleaned titanium (Ti) foil (80 mm × 20 mm) with a much larger surface area and immersed it in the autoclave, which could collect much more Co_3O_4 powders for the BET detection. The autoclave was sealed and maintained in an electric oven at 95 °C for 24 h. After cooling down to room temperature, the substrate was removed, rinsed with distilled water several times in order to remove the free standing nanoparticles or residual reactant, and dried at 60 °C under vacuum for 2 h. After that, the as-prepared pink precursors of $Co(CO_3)_{0.5}(OH) \cdot 0.11H_2O$ were converted to Co_3O_4 *via* thermal decomposition at 500 °C in air for another 4 h. After the fabrication of Co_3O_4 NWs, TiO_2 nanoparticles were modified on the surface of Co_3O_4 by using PLD. The TiO_2 ceramic target applied in PLD was sintered at 1300 °C using the TiO_2 (5 N) powder directly. The target was placed at a distance of 4.5 cm from the substrate during deposition and a KrF excimer laser (Compex 102, 248 nm, 5 Hz) was used as the ablation source. Prior to the deposition, the chamber was evacuated to a low pressure of $\sim 10^{-4}$ Pa. Then pure O_2 (99.999%) was introduced as the working gas with a pressure of 10 Pa. The TiO_2 nanoparticles were fabricated at 500 °C with a typical radius of about 5–20 nm.

The structure of the sample was characterized by using a Bede D1 X-ray diffraction (XRD) system with Cu Kα radiation (λ = 0.15406 nm). Surface morphology of the sample and its element contents were studied by using an FEI Quanta 200F scanning electron microscope (SEM) operated at a voltage of 20 kV equipped with an energy-dispersive X-ray spectrometer (EDX). An X-ray photoelectron spectrometer (XPS, Thermo Fisher K-Alpha American with an Al Kα X-ray source) was also used to measure the elemental composition of samples. Specific surface areas of the samples were obtained from the results of N_2 adsorption–desorption isotherms at 77 K (Micromeritics ASAP 3020) by using the Brunauer–Emmett–Teller (BET) method. The structure of the sample was identified by using an FEI Tecnai G2 F20 transmission electron microscope (TEM) equipped with a selected area electron diffractometer (SAED) and a scanning transmission electron microscope (STEM), which was operated at 200 kV. Microscopic Raman spectroscopy was carried out by using a micro-Raman spectrometer (InVia Reflex, Renishaw, UK) with an excitation wavelength of 532 nm, and the laser power was kept below 0.85 mW to avoid the laser induced heating effect on the sample. All peaks in the Raman spectra were fitted with Lorentzians. A 100× objective lens with a numerical aperture (NA) of 0.95 was used in the Raman experiments, and the spot size was estimated to be about 500 nm. Thermogravimetric analysis (TGA, SDT Q600) was carried out under an air atmosphere at 10 °C min^{-1} with a temperature range of 10–900 °C.

The gas sensing experiment of the samples was performed on an intelligent gas sensing analysis system (CGS-1TP, Beijing Elite Tech Co., Ltd, China), which provided an external and precious temperature control from room temperature to 500 °C with a minimum step of 1 °C. Prior to the experiment, the sensors were pre-heated at different temperatures for about 30 min. When the resistance of the sensor was stable, the target gas was injected into the chamber using a micro-injector through a rubber plug. The gas response was designated as R_g/R_a, where R_g is the sensor resistance measured in a mixture of target gases and R_a is the resistance of the sample measured in air. The detailed gas-sensing experiment process can be found in the previous report by Wen *et al.*[12]

3. Results and discussion

The fabrication process of TiO_2/Co_3O_4 acicular NW arrays is schematically illustrated in Fig. 1. First, Co related precursor arrays were obtained by a hydrothermal method using the $Co(NO_3)_2 \cdot 4H_2O$, NH_4F, and $CO(NH_2)_2$ as sources at 95 °C for 12 h. And then, the precursor was converted to uniform porous acicular Co_3O_4 NW arrays *via* calcination at 500 °C for 4 h. The detailed formation process of the TiO_2/Co_3O_4 acicular NW

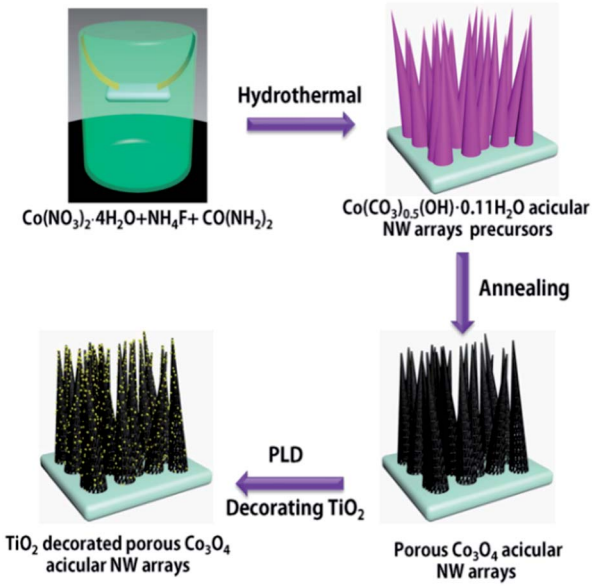

Fig. 1 Schematic diagram of the fabrication process.

arrays is illustrated in the ESI.† Finally, uniform TiO_2/Co_3O_4 NW acicular arrays could be obtained after decorating TiO_2 nanoparticles on its surface by using PLD.

Fig. 2 shows the XRD patterns of the as-synthesized precursor (a), Co_3O_4 NW arrays (b) and TiO_2/Co_3O_4 NW arrays (c), respectively. In the XRD pattern of the as-synthesized precursor, excluding those peaks arising from the substrate, all of the peaks are in good agreement with the $Co(CO_3)_{0.5}(OH){\cdot}0.11H_2O$ (JCPDS PDF#48-0083). In the XRD pattern of the annealed precursor, all the diffraction peaks can be indexed to the face-centered cubic Co_3O_4 (JCPDS PDF#43-1003), which confirms the complete conversion from cobalt carbonate hydroxide to Co_3O_4. According to the XRD pattern of TiO_2/Co_3O_4, all of the observed diffraction peaks correspond to the Co_3O_4 and Al_2O_3 substrates. No obvious TiO_2 related peaks were found in the XRD pattern of the TiO_2/Co_3O_4, probably owing to the small content of TiO_2 in the nanocomposites.

The morphology of the TiO_2/Co_3O_4 NW arrays was characterized by SEM, as shown in Fig. 3. In Fig. 3(a), large scale, high density and acicular like TiO_2/Co_3O_4 arrays are found to deposit uniformly on the substrate. In the cross-sectional SEM image of TiO_2/Co_3O_4 in Fig. 3(b), the TiO_2/Co_3O_4 acicular NW arrays are homogeneously aligned on the substrate, and the length of Co_3O_4 NW arrays was about 1–3 μm. Fig. 3(c) demonstrates a typical SEM image of the TiO_2 decorated Co_3O_4 acicular NW arrays in a high magnification, in which obvious acicular like Co_3O_4 NWs are observed. In this study, it is found that the growth temperature plays a significant role in affecting the morphologies of the as-prepared precursor, which is discussed in detail in Fig. S1.† Fig. 3(d) shows the EDX information of the TiO_2/Co_3O_4, confirming the coexistence of Ti, Co and O. Fig. S2† demonstrates a top view of the pristine Al_2O_3 substrate, the precursors of $Co(CO_3)_{0.5}(OH){\cdot}0.11H_2O$, the as-prepared Co_3O_4 acicular NW arrays and the TiO_2/Co_3O_4. The surface of the substrate would be covered with pink precursors after the hydrothermal reaction, which can be fully converted to the black Co_3O_4 *via* the thermal decomposition process. There are no obvious colour differences between the as-prepared Co_3O_4 acicular NW arrays and the TiO_2/Co_3O_4.

The TEM images of the as-prepared $Co(CO_3)_{0.5}(OH){\cdot}0.11H_2O$ precursor, Co_3O_4 NW, and TiO_2/Co_3O_4 NW are compared in Fig. 4(a)–(c), respectively. All of them display an obvious acicular like structure. No obvious macroscopic defects were found in the as-prepared $Co(CO_3)_{0.5}(OH){\cdot}0.11H_2O$, as shown in Fig. 4(a). While after annealing, plenty of nanopores were formed in the Co_3O_4 NW, which may be generated due to the dehydration and lattice contraction occurring during the thermal treatment (Fig. 4(b)). After the deposition of TiO_2, the acicular morphology of the Co_3O_4 does not demonstrate obvious changes, as shown

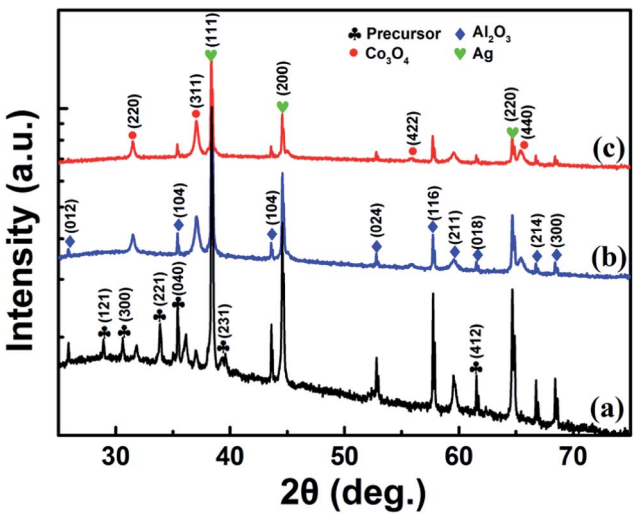

Fig. 2 XRD patterns of the (a) as-synthesized precursor, (b) pristine Co_3O_4 NW arrays and (c) TiO_2/Co_3O_4 NW arrays.

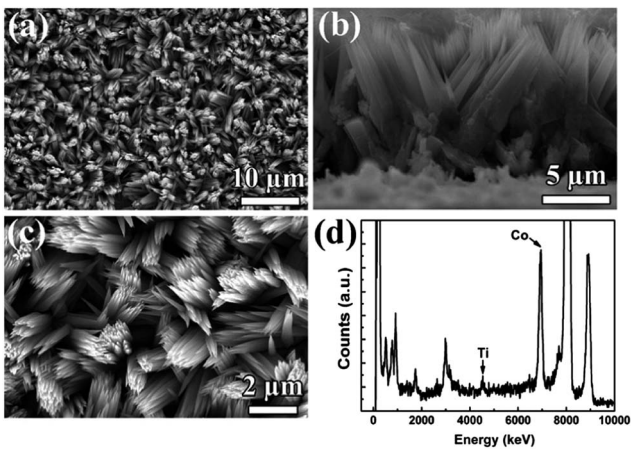

Fig. 3 The morphology and content of the TiO_2/Co_3O_4 NW arrays. (a) SEM image of TiO_2/Co_3O_4 NW arrays deposited on the Al_2O_3 substrate. (b) The cross-sectional SEM image of TiO_2/Co_3O_4 NW arrays. (c) SEM image of TiO_2/Co_3O_4 NW arrays at a high magnification. (d) The EDX information of the TiO_2/Co_3O_4.

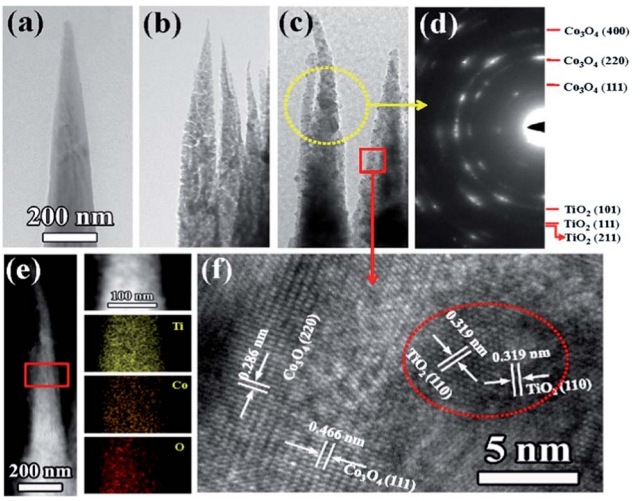

Fig. 4 The TEM images of the as-prepared $Co(CO_3)_{0.5}(OH)\cdot 0.11H_2O$ precursor, Co_3O_4 NW, and TiO_2/Co_3O_4 NW are compared in (a)–(c) respectively. (d) SAED pattern of the TiO_2/Co_3O_4 NW collected from the yellow circle. (e) A STEM image and the element distribution of the TiO_2/Co_3O_4. (f) A HRTEM image of the TiO_2/Co_3O_4 NW.

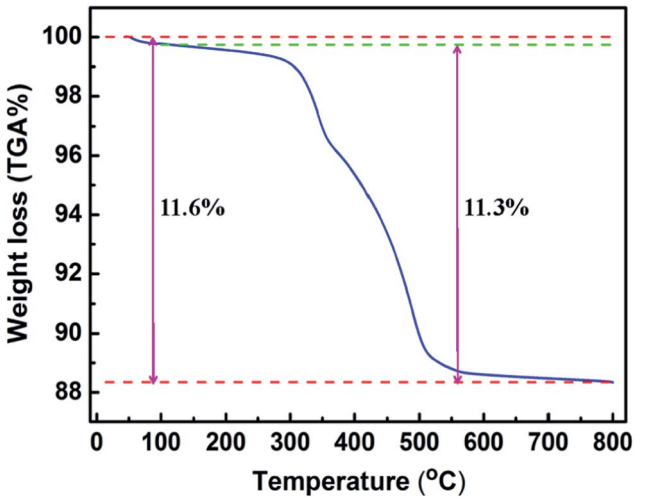

Fig. 5 The thermodecomposition behavior of the $Co(CO_3)_{0.5}(OH)\cdot 0.11H_2O$, which was characterized by using TGA in air.

in Fig. 4(c). Because of so many nanopores existing in the Co_3O_4 NW, leading to a large surface area, it is supposed to be a good structure for gas sensing. N_2 sorption was used for characterizing the porous structure of acicular Co_3O_4 NW arrays (Fig. S3†). Its isotherm has a typical character of IV type loop, indicating the mesoporous structure.[29] The BET surface areas of Co_3O_4 NW arrays are calculated to be ~22 $m^2\ g^{-1}$, and the pore size distribution shows a peak located at 18.5 nm, while that of the as-prepared precursor is only ~3 $m^2\ g^{-1}$. Although the substrate also plays a significant role in controlling the kinetics of the growth, we succeeded in producing the Co_3O_4 NW arrays with an acicular structure on the Ti foil (Fig. S4†). Thus in this study, we can select Ti foil as the substrate for collecting more powders for BET characterization, which has been applied in our previous studies.[13] Fig. 4(e) shows the STEM image of the TiO_2/Co_3O_4, from which it is found that the TiO_2 nanoparticles are uniformly decorated on the surface of Co_3O_4. The circles in the SAED patterns were attributed to TiO_2 (101), TiO_2 (111), TiO_2 (211), Co_3O_4 (111), Co_3O_4 (220), and Co_3O_4 (400). The high-resolution TEM (HRTEM) image in Fig. 4(f) reveals that the lattice fringes of 0.319 nm, 0.286 nm and 0.466 nm can be assigned to the existence of TiO_2 (110), Co_3O_4 (220), and Co_3O_4 (111), respectively.

Fig. 5 shows the thermodecomposition behavior of $Co(CO_3)_{0.5}(OH)\cdot 0.11H_2O$, which was characterized by using TGA. It is found that there exist three apparent decomposition steps: the first one appears when the temperature is below 80 °C, during which the weight loss is mainly due to the evaporation of adsorbed water. The second turning point appears at 350 °C, which may be due to the decomposition of the residual reactant $Co(NO_3)_2$. The third turning point appears at 500 °C, corresponding to conversion from $Co(CO_3)_{0.5}(OH)\cdot 0.11H_2O$ to Co_3O_4. During the oxidation process of the precursor, a weight loss of ~11.6% was found. Thus, in order to improve the stabilization of the gas sensor in a long term application, all of the samples were annealed at 500 °C.

In order to investigate the chemical composition of the prepared TiO_2/Co_3O_4, XPS measurement was carried out (Fig. 6). During the XPS analysis, the C 1s peak located at 284.5 eV was selected as the reference. Fig. 6(a) shows a full survey scan spectrum of the TiO_2/Co_3O_4 NW arrays, and two peaks located at 780.2 and 795.6 eV are related to the Co $2p_{3/2}$ and Co $2p_{1/2}$, which corresponds to the standard Co_3O_4 spectra, as seen in Fig. 6(b).[9,27,30] Similarly, the peaks appearing at 457.5 eV and 463.4 eV in Fig. 6(c) are ascribed to the Ti $2p_{3/2}$ and Ti $2p_{1/2}$ for a typical TiO_2.[2] And subsequently, the O 1s core-level spectra of the as-prepared series of samples were studied, as shown in Fig. 6(d). On comparison of the data on the spectra of other related studies, the lowest BE component located at 530 eV (referred to as O_{intr}) is attributed to O^{2-} ions in the structure of

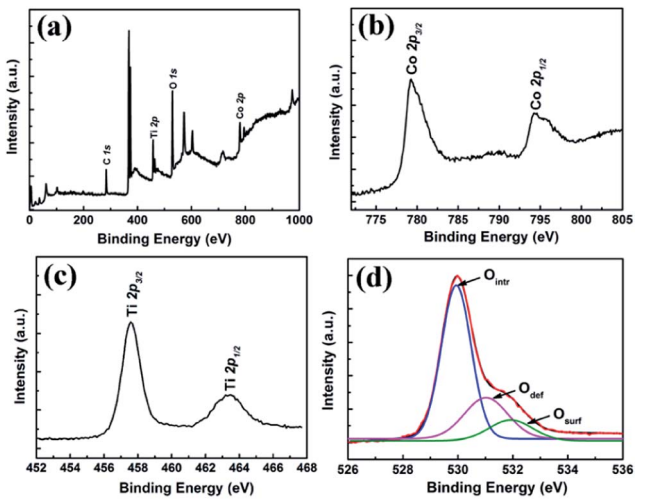

Fig. 6 (a) XPS spectra of the TiO_2/Co_3O_4. (b) An enlarged spectra of Co 2p, (c) Ti 2p, and (d) O.

the Co_3O_4 and TiO_2 array. While the middle one located at 531 eV (referred to as O_{def}) is attributed to O^{2-} ions that are in oxygen deficient regions. And the higher BE peak located at 532 eV (referred to as O_{surf}) is due to the presence of other adsorption states such as H–O bonds or loosely bound oxygen on the surface.[3,31,32] From the XPS pattern of the TiO_2/Co_3O_4, it further confirms that the as-prepared sample is composited with Co_3O_4 and TiO_2.

The Raman spectra of the Co_3O_4 and TiO_2/Co_3O_4 NW arrays are shown in Fig. 7. The vibration bands located at 475, 516, 615, and 680 cm^{-1} in the Raman spectrum are attributed to the Co_3O_4, while the vibration bands appeared at 396, 516, and 639 cm^{-1} are attributed to the TiO_2.[2] After decorating with TiO_2, the Raman vibration bands of Co_3O_4 are broadened, which may be due to the interaction between the TiO_2 and Co_3O_4 and the disorder in the sublattice.

During the gas sensing measurement, 100 ppm of ethanol was introduced into a sealed chamber and the sample was heated up to an optimal temperature. The gas-sensing measurements were performed on an intelligent gas sensing analysis system, which is shown in Fig. S5.† The current–voltage (*I–V*) characteristics of the sample verified the ohmic contacts between the Co_3O_4 nanowire arrays and the electrodes (Fig. S6†). In order to find the optimal working temperature of the sample, the maximum responses to ethanol for the Co_3O_4 and TiO_2/Co_3O_4 at a series of working temperatures are studied. In Fig. 8(a), all of the samples demonstrate an enhanced gas response with increasing working temperature, and then they decrease when the temperature is higher than the optimal one. The optimal working temperatures of the Co_3O_4 and TiO_2/Co_3O_4 are 170 °C and 160 °C, respectively. The gas sensing behaviour can be explained according to the kinetics and mechanics of gas adsorption and desorption on the surface of Co_3O_4. When the operating temperature is too low, not enough chemical activations (such as OH^-, CO_3^{2-}, COO^-, *etc.*) of gas-sensing materials are generated,[33,34] leading to a small response. By increasing the temperature, the driving force for desorption of O_2 is increased, contributing to an increase of the response. When the operating temperature is too high (higher than the optimal working temperature), O_2 adsorbed on the surface may quickly escape before their reaction, thus the response will decrease correspondingly. A sensor can demonstrate its maximum gas sensing performance only at the optimal working temperature. Fig. 8(b) compares the response characteristic curves of these two sensors at the optimal temperatures. It shows that the gas response of the TiO_2/Co_3O_4 ($R_g/R_a = 65$) sensor to 100 ppm of ethanol is much higher than that of the pristine Co_3O_4 ($R_g/R_a = 25$), which indicates that the interaction between the TiO_2 and Co_3O_4 can effectively improve its gas sensing ability. The superiority of the p–n junction sensor to the conventional chemi-resistive sensor is illustrated in the ESI (Fig. S7†). As reported previously, TiO_2 is not a good gas sensing material,[35] so an optimal content of TiO_2 deposited on Co_3O_4 may play a significant role in affecting its response. The gas responses of the TiO_2/Co_3O_4 sensor to a series of TiO_2 contents are shown in Fig. S8.† It is found that the TiO_2

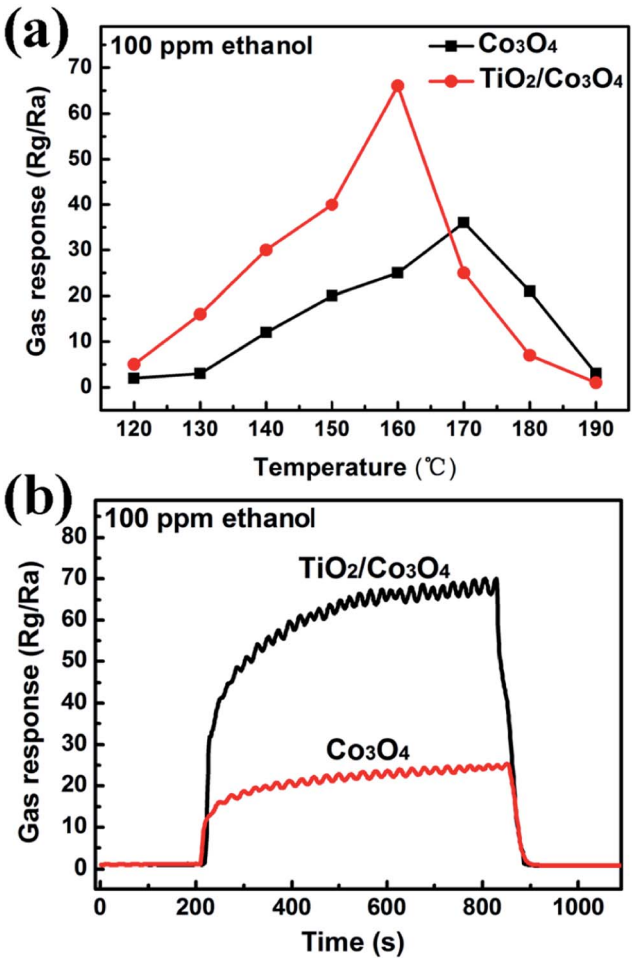

Fig. 8 (a) Response *versus* working temperature of the Co_3O_4 and TiO_2/Co_3O_4 sensor exposed to 100 ppm ethanol and (b) the typical response curve of the Co_3O_4 and TiO_2/Co_3O_4 sensor to 100 ppm ethanol at a working temperature of 160 °C.

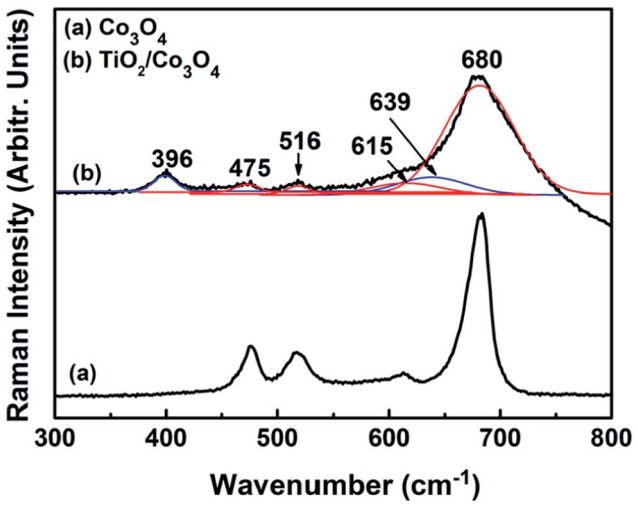

Fig. 7 Raman spectra of the pristine Co_3O_4 and TiO_2/Co_3O_4 NW arrays.

deposited by PLD for 20 s contributes to the maximum gas response for 100 ppm of ethanol.

Not only enhancing the maximum value of gas response, the TiO_2/Co_3O_4 sensor also displays a good response to a series of concentrations of ethanol. As shown in Fig. 9(a), the responses of the TiO_2/Co_3O_4 sensor follow an almost linear increase with the increase of ethanol concentration from 10 ppm to 500 ppm, indicating its good response to ethanol over a wide range. In order to confirm that the TiO_2/Co_3O_4 sensor displays an obviously enhanced sensing ability compared to the pristine Co_3O_4, the gas responses of the Co_3O_4 and TiO_2/Co_3O_4 to a series of concentrations of ethanol are compared in Fig. S9.† It is found that the TiO_2/Co_3O_4 sensor always displays a higher response than the pristine Co_3O_4 to the same concentration of ethanol.

Moreover, the reproducibility performance of the sensor is also measured. Fig. 9(b) shows that the on and off responses of Co_3O_4 could be repeated after continuous measurement without obvious changes, showing that the sensor based on TiO_2/Co_3O_4 has good reversibility and stability. In order to confirm the selectivity behavior of the sensor, we select some other gases such as NH_3, benzene, acetone and methanol to characterize its sensing activities (Fig. S10†). The responses of the sensor to these gases with a concentration of 100 ppm were determined at 160 °C. The gas response to 100 ppm ethanol is 65, which is significantly higher than acetone and methanol. Meanwhile, it shows a pretty low response to NH_3 and benzene. The significant gas response difference indicates the selectivity of the TiO_2/Co_3O_4 sensor.

The on and off gas response process can be explained by gas adsorption, surface chemical reaction and desorption, which lead to significant electrical conductivity changes resulting from the chemical interaction of gas molecules with the oxygen species on its surface.[26] At the optimal operating temperature, the adsorption of negatively charged oxygen can generate plenty of holes for the conduction, which leads to the formation of a charge accumulation layer on the surface of Co_3O_4. When the sensor is exposed to ethanol, the oxygen species on Co_3O_4 could promote the oxidation of ethanol gas molecules to CO_2 and H_2O. Meanwhile, it also releases plenty of extra electrons, which would neutralize the holes existing in the Co_3O_4, as a result, its resistance demonstrates a dynamic increase.

Herein, a typical p–n heterojunction is formed when n-type TiO_2 is decorated on p-type Co_3O_4, which greatly improves its gas sensing response. Based on the calculation and experiment reported previously,[35] the energy band structure diagram for the p-type Co_3O_4/n-type TiO_2 heterojunction is described in Fig. 10. In the heterogeneous region, the holes in p-type semiconductor Co_3O_4 and the electrons in the n-type semiconductor TiO_2 form a self-built electric field, which could establish a depletion layer until they get an equalization of the Fermi level. The heterojunction region of TiO_2/Co_3O_4 is believed to easily attract reductive and oxidative gases. When exposed to air (1), the hole density on the surface of Co_3O_4 increases while the number of electrons on the surface of TiO_2 decreases due to the ionization of absorbed oxygen species, during which the holes can easily transfer to the p-type Co_3O_4 semiconductor, leading to a lower resistance of the sensor.

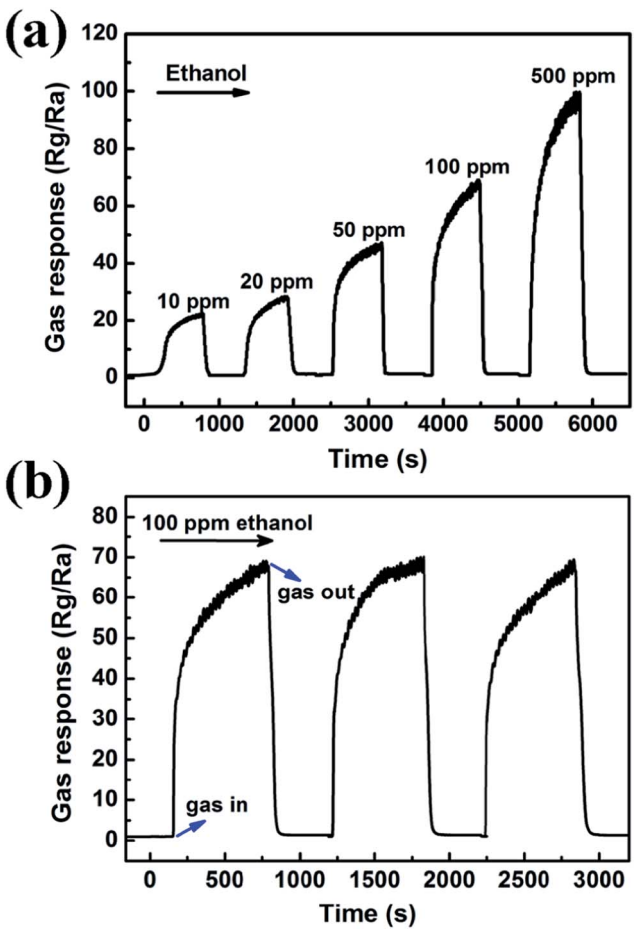

Fig. 9 (a) Response of the TiO_2/Co_3O_4 sensor to a series of concentrations of ethanol at 160 °C. (b) The typical response and recovery curve of the TiO_2/Co_3O_4 sensor between 100 ppm ethanol and ambient air.

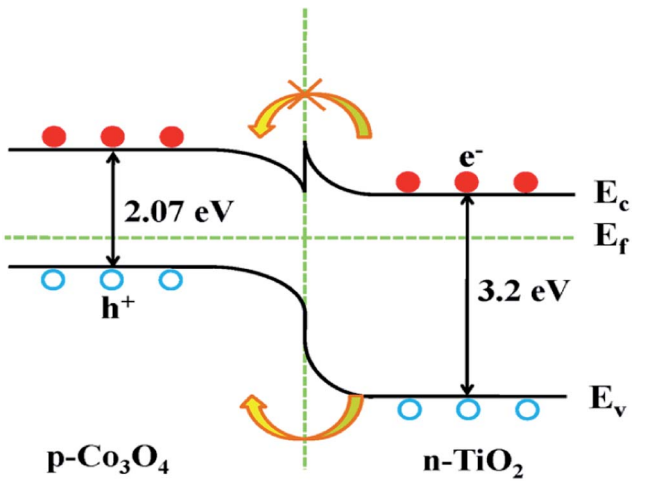

Fig. 10 The energy band structure diagram for the p-type Co_3O_4/n-type TiO_2 heterojunction.

$$1/2O_2\ (g) \rightarrow O^-\ (ads) + h^* \quad (1)$$

When ethanol was introduced into the chamber, the charge carrier accumulation layer near the surface is thinned by the electrochemical interaction between O^- (ads) and C_2H_5OH molecules (2), which releases free electrons and neutralizes the holes in the Co_3O_4. But at this moment, the electron transfer from the n-type semiconductor to the p-type semiconductor is impeded, which makes the resistance of the device increase rapidly. As a consequence, the TiO_2/Co_3O_4 demonstrates a higher gas sensitivity than the pristine Co_3O_4. The reaction process can be described as follows:

$$C_2H_5OH\ (g) + 6O^-\ (ads) \rightarrow 2CO_2\ (g) + 3H_2O\ (g) + 6e^- \quad (2)$$

When the ethanol flow stopped, oxygen molecules in air could be adsorbed onto the surface of the Co_3O_4 again. Consequently, its resistance returns to its initial value.

4. Conclusion

In summary, TiO_2/Co_3O_4 arrays have been synthesized on the Ag/Pd electrode substrate by combining hydrothermal and PLD methods. The structure and morphology of TiO_2/Co_3O_4 were characterized by XRD, TEM, STEM, XPS, and Raman spectroscopy, which confirm that TiO_2 nanoparticles were uniformly decorated on the surface of Co_3O_4. The heterojunction structure of TiO_2/Co_3O_4 displayed enhanced sensing ability to ethanol by almost three times compared with pristine Co_3O_4, which is due to the formation of the p–n junction between the p-type Co_3O_4 and the n-type TiO_2. The self-built electric field originating from the p–n junction effect can enhance the thickness of the depletion layer, which improves its gas sensitivity. Our study has evidently confirmed that the surface modification is an effective approach to enhance the sensing performance of the ethanol sensor.

Acknowledgements

This work was financially supported by the Beijing Natural Science Foundation of China (no. 2144054), National Natural Science Foundation of China (nos 21322609, 21106184, 21207144, 51401239, and 11404138), Key Program Project of National Natural Science Foundation of China (51231008), Science Foundation of China University of Petroleum, Beijing (nos YJRC-2013-40, QZDX-2014-01), the Key Project of Chinese Ministry of Education (313055), the National 973 program of China (2012CB619403), and Thousand Talents Program of China.

References

1 J.-W. Wen, D.-W. Zhang, Y. Zang, X. Sun, B. Cheng, C.-X. Ding, Y. Yu and C.-H. Chen, *Electrochim. Acta*, 2014, **132**, 193–199.
2 J. Li, G. Lu, G. Wu, D. Mao, Y. Guo, Y. Wang and Y. Guo, *Catal. Sci. Technol.*, 2014, **4**, 1268–1275.
3 Y. S. Luo, J. S. Luo, W. W. Zhou, X. Y. Qi, H. Zhang, D. Y. W. Yu, C. M. Li, H. J. Fan and T. Yu, *J. Mater. Chem. A*, 2013, **1**, 273–281.
4 S. L. Xiong, C. Z. Yuan, M. F. Zhang, B. J. Xi and Y. T. Qian, *Chem.–Eur. J.*, 2009, **15**, 5320–5326.
5 Y. Y. Liang, Y. G. Li, H. L. Wang, J. G. Zhou, J. Wang, T. Regier and H. J. Dai, *Nat. Mater.*, 2011, **10**, 780–786.
6 X. W. Xie, Y. Li, Z. Q. Liu, M. Haruta and W. J. Shen, *Nature*, 2009, **458**, 746–749.
7 L. Wang, J. Deng, Z. Lou and T. Zhang, *Sens. Actuators, B*, 2014, **201**, 1–6.
8 A. M. Cao, J. S. Hu, H. P. Liang, W. G. Song, L. J. Wan, X. L. He, X. G. Gao and S. H. Xia, *J. Phys. Chem. B*, 2006, **110**, 15858–15863.
9 Q. Z. Jiao, M. Fu, C. You, Y. Zhao and H. S. Li, *Inorg. Chem.*, 2012, **51**, 11513–11520.
10 J.-W. Yoon, J.-K. Choi and J.-H. Lee, *Sens. Actuators, B*, 2012, **161**, 570–577.
11 V. Balouria, S. Samanta, A. Singh, A. K. Debnath, A. Mahajan, R. K. Bedi, D. K. Aswal and S. K. Gupta, *Sens. Actuators, B*, 2013, **176**, 38–45.
12 Z. Wen, L. P. Zhu, W. M. Mei, L. Hu, Y. G. Li, L. W. Sun, H. Cai and Z. Z. Ye, *Sens. Actuators, B*, 2013, **186**, 172–179.
13 Z. Wen, L. P. Zhu, W. M. Mei, Y. G. Li, L. Hu, L. W. Sun, W. T. Wan and Z. Z. Ye, *J. Mater. Chem. A*, 2013, **1**, 7511–7518.
14 N. Chen, X. Li, X. Wang, J. Yu, J. Wang, Z. Tang and S. A. Akbar, *Sens. Actuators, B*, 2013, **188**, 902–908.
15 J. Feng and H. C. Zeng, *Chem. Mater.*, 2003, **15**, 2829–2835.
16 M. Nishibori, W. Shin, N. Izu, T. Itoh and I. Matsubara, *Catal. Today*, 2013, **201**, 85–91.
17 A. D. Khalaji, M. Nikookar, K. Fejfarova and M. Dusek, *J. Mol. Struct.*, 2014, **1071**, 6–10.
18 H. Guan, C. Shao, S. Wen, B. Chen, J. Gong and X. Yang, *Mater. Chem. Phys.*, 2003, **82**, 1002–1006.
19 P. N. Shelke, Y. B. Khollam, R. R. Hawaldar, S. D. Gunjal, R. R. Udawant, M. T. Sarode, M. G. Takwale and K. C. Mohite, *Fuel*, 2013, **112**, 542–549.
20 M. Pudukudy and Z. Yaakob, *Chem. Pap.*, 2014, **68**, 1087–1096.
21 X. F. Lu, C. Wang and Y. Wei, *Small*, 2009, **5**, 2349–2370.
22 A. K. Chakraborty, S. Akter, M. A. Haque, G. M. A. Khan and M. S. Alam, *J. Cluster Sci.*, 2013, **24**, 701–713.
23 G. P. Dai, S. Q. Liu, Y. Liang and T. X. Luo, *Appl. Surf. Sci.*, 2013, **264**, 157–161.
24 M. C. Long, W. M. Cai and H. Kisch, *J. Phys. Chem. C*, 2008, **112**, 548–554.
25 R.-J. Wu, J.-G. Wu, M.-R. Yu, T.-K. Tsai and C.-T. Yeh, *Sens. Actuators, B*, 2008, **131**, 306–312.
26 Y. Liu, G. Zhu, J. Chen, H. Xu, X. Shen and A. Yuan, *Appl. Surf. Sci.*, 2013, **265**, 379–384.
27 D. Bekermann, A. Gasparotto, D. Barreca, C. Maccato, E. Comini, C. Sada, G. Sberveglieri, A. Devi and R. A. Fischer, *ACS Appl. Mater. Interfaces*, 2012, **4**, 928–934.
28 C. W. Na, H. S. Woo, I. D. Kim and J. H. Lee, *Chem. Commun.*, 2011, **47**, 5148–5150.

29 L. P. Zhu, Z. Wen, W. M. Mei, Y. G. Li and Z. Z. Ye, *J. Phys. Chem. C*, 2013, **117**, 20465–20473.
30 Y.-W. Chen, H.-J. Chen and D.-S. Lee, *J. Mol. Catal. A: Chem.*, 2012, **363–364**, 470–480.
31 C. L. Cao, C. G. Hu, W. D. Shen, S. X. Wang, J. L. Wang and Y. S. Tian, *J. Alloys Compd.*, 2013, **550**, 137–143.
32 L. Q. Zhang, Z. Z. Ye, J. G. Lu, B. Lu, Y. Z. Zhang, L. P. Zhu, J. Zhang, D. Yang, K. W. Wu, J. Huang and Z. Xie, *J. Phys. D: Appl. Phys.*, 2010, **43**, 015001.
33 M. Ghasdi and H. Alamdari, CO sensitive nanocrystalline $LaCoO_3$ perovskite sensor prepared by high energy ball milling, *Sens. Actuators, B*, 2010, **148**, 478–485.
34 N. Yamazoe, J. Fuchigami, M. Kishikawa and T. Seiyama, Interactions of tin oxidesurface with O_2, H_2O and H_2, *Surf. Sci.*, 1979, **86**, 335–344.
35 Y. Q. Liang, Z. D. Cui, S. L. Zhu, Z. Y. Li, X. J. Yang, Y. J. Chen and J. M. Ma, *Nanoscale*, 2013, **5**, 10916–10926.